UNIVERSITY OF NAPLES FEDERICO II

DOCTORATE IN
MOLECULAR MEDICINE AND MEDICAL BIOTECHNOLOGY

XXXIV CYCLE

Barbara Carrese

CHEMO- PHOTOTHERMAL AND PHOTODYNAMIC THERAPIES FOR CANCER TREATMENT

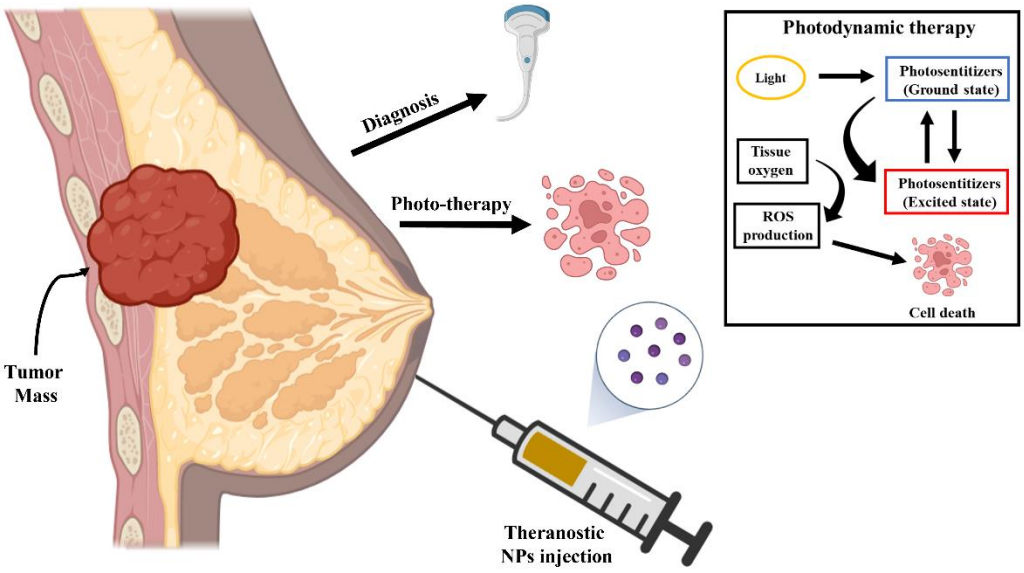

2019-2023

UNIVERSITY OF NAPLES FEDERICO II

DOCTORATE IN
MOLECULAR MEDICINE AND MEDICAL BIOTECHNOLOGY

XXXV CYCLE

CHEMO- PHOTOTHERMAL AND PHOTODYNAMIC THERAPIES FOR CANCER TREATMENT

Tutor
Prof. Annalisa Lamberti

Candidate
Barbara Carrese

2019-2023

Table of contents

List of Abbreviations used	III
Abstract	V
1. Background	1
1.1 Nanoparticles	1
1.2 Drug delivery	2
1.2.1 Passive targeting delivery	2
1.2.2 Active targeting delivery	3
1.3 Albumin and SPARC	4
1.4 Multi-drug resistance	6
1.5 Nanotheranostics for targeted diagnosis and therapy	7
1.6 Eumelanin	11
1.7 Breast cancer	11
1.7.1 Triple-negative breast cancer	12
1.8 Melanoma	13
1.9 Chemotherapy	14
1.9.1 Doxorubicin	14
1.9.2 Ru(II) complexes	15
1.10 Phototherapy	17
1.10.1 Photothermal therapy	17
1.10.2 Photodynamic therapy	18
1.11 Photoacoustic effect and photoacoustic imaging	19
2. Aims of thesis	21
3. Materials and Methods	22
3.1 Reagents	22
3.2 Cell culture	22
3.3 HSA-DOX quenching effect	22
3.4 Stern–Volmer plots	22
3.5 Evaluation of HSA amount bonded to MelaSil_Ag NPs	23
3.6 Loading of DOX to MelaSil_Ag-HSA NPs	23
3.7 Dynamic light scattering and ζ-potential characterization	24
3.8 DOX release from MelaSil_Ag-HSA@DOX NPs	24
3.9 Confocal microscopy of 2D cells	24
3.10 Cell viability assays	24
3.11 Photothermal response of MelaSil_Ag NPs under CW laser irradiation	25
3.12 Cell viability following laser irradiation	26
3.13 Spheroid formation	26
3.14 Confocal and Thunder microscopy of 3D model	26
3.15 Morphological changes in HS578T spheroids	27
3.16 Cell viability in 3D HS578T model	27
3.17 Photophysical properties of the synthesized ruthenium (II) complexes	27

3.18 DNA cleavage 28
3.19 Caspases activity 28
3.20 ROS detection 29
3.21 Statistical Analysis 29
4. Results 30
4.1 Evaluation of MelaSil_Ag-HSA@DOX NPs cytotoxicity in 2D and 3D models 30
4.1.1 Doxorubicin and human serum albumin interaction 30
4.1.2 DOX and MelaSil_Ag-HSA nanoparticles interaction 31
4.1.3 Drug loading on MelaSil_Ag-HSA NPs 32
4.1.4 Drug release 33
4.1.5 DOX delivery in breast cancer cells 34
4.1.6 Cytotoxicity of MelaSil_Ag-HSA@DOX NPs vs. free DOX in 2D cells 35
4.1.7 Thermal properties of MelaSil_Ag-HSA NPs 37
4.1.8 Thermal trend of DMEM and DOX 38
4.1.9 Cytotoxicity of MelaSil_Ag-HSA@DOX upon laser irradiation 39
4.1.10 Evaluation of bare and HSA-NPs uptake in HS578T and MCF10a spheroids 40
4.1.11 DOX delivery in HS578T spheroids 42
4.1.12 Morphological changes of HS578T spheroids after treatment with DOX@NPs 43
4.1.13 Cell viability assay of DOX@NPs 44
4.2 Characterization of new Ruthenium complexes 45
4.2.1 Photophysical properties of the synthesized ruthenium (II) complexes 45
4.2.2 Ruthenium-mediated photosensitizing DNA cleavage 47
4.2.3 Cell viability assays 48
4.2.4 Caspases activity 51
4.2.5 Reactive oxygen species detection assay 53
5. Discussion 54
6. Conclusions 61
7. Acknowledgements 62
8. List of publications 63
9. References 64

List of Abbreviations used

ABCD	Asymmetry, Border irregularity, Color variation, Diameter
AFT	Albumin Fusion Technology
APTES	3-(aminopropyl) triethoxysilane
BC	Breast Cancer
BM-40	Base-Membrane Protein-40
CAs	Contrast Agents
CDKN2A	Cyclin-Dependent Kinase Inhibitor 2A
CW	Continuous Wavelength
DHI	5,6-dihydroxyindole
DHICA	5,6-dihydroxyindole-2-carboxylic acid
DLS	Dynamic Light Scattering
DOX	Doxorubicin
DOXO-EMCH	6-maleimidocaproyl hydrazone derivative of doxorubicin
ECM	Extracellular Matrix
EDC	1-ethyl-3-(3-dimethylaminopropyl) carbodiimide
EPR	Enhanced Permeability Retention
ER	Estrogen Receptor
FBS	Fetal Bovine Serum
FHS	Fetal Horse Serum
FTIR	Fourier-Transform Infrared Spectroscopy
HER2	Human Epidermal Growth Factor Receptor 2
HSA	Human Serum Albumin
i.v.	Intravenously
MDR	Multi-drug Resistance
MRI	Magnetic Resonance Imaging
MFI	Mean Fluorescence Intensity
NHS	N-hydroxysuccinimide
NIR	Near-Infrared
NPs	Nanoparticles
ON	Overnight
PA	Photoacoustic
PAI	Photoacoustic Imaging
PAS	Photoacoustic Signal
PBS	Phosphate-Buffered Saline
PDI	Poly Dispersion Index
PDT	Photodynamic Therapy
PFA	Paraformaldehyde
PHS	Photo-Stability

PI	Propidium Iodide
PR	Progesterone Receptor
PS	Photosensitizer
PTT	Photothermal Therapy
ROS	Reactive Oxygen Species
RuPOPs	Ruthenium(II) polypyridyl complexes
SEM	Scanning Electron Microscopy
SPARC	Secreted Protein Acidic and Rich in Cysteine
TCA	Trichloroacetic Acid
TEM	Transmission Electron Microscopy
TNBC	Triple-Negative Breast Cancer

3. Materials and Methods

3.1 Reagents

3.2 Cell culture

Human breast carcinoma cell line (HS578T), human melanoma cell line (A375) and mammary breast fibrocystic disease cell line (MCF10a) were obtained from the American Type Tissue Collection (Rockville, MD, USA). HS578T and A375 cells were grown in DMEM supplemented with 10% heat inactivated Fetal Bovine Serum (FBS) (GIBCO), 100 U/mL penicillin, 100 mg/mL streptomycin, and 1% L-glutamine. MCF10a cells were grown in MEGM (Lonza, Basel, Switzerland) supplemented with Mammary Epithelial Cell Growth Medium Bullet Kit (Lonza), 100 nM cholera toxin (Sigma-Aldrich) and 5% heat inactivated Fetal Horse Serum (FHS) (Lonza). All cell lines were grown at 37°C in a 5% CO_2 atmosphere.

3.3 HSA-DOX quenching effect

Human serum albumin (10 µM) was incubated with DOX at increasing molar ratio HSA:DOX (1:5, 1:15, 1:20, and 1:40) in PBS 1× pH 7.4 for 24h under stirring at room temperature (RT). The HSA fluorescence spectra were recorded with an excitation wavelength of 280 nm and collected from 287 to 500 nm. All measurements were carried out in triplicate in three independent experiments.

3.4 Stern–Volmer plots

To study the interaction between HSA and DOX and to calculate the dissociation constant (K_d), the quenching constant (k_q), and the number of binding sites (*n*), Stern– Volmer plot analysis was performed. In brief, to calculate the K_d and k_q values, HSA fluorescence intensity at 347 nm (typical of tryptophan residues) was plotted as the ratio between fluorescence in the absence (F0) and in the presence (F) of the quencher (DOX) at various concentrations (50, 150, 200, 400 µM) versus the molar concentrations of DOX. From the linear regression, the Stern–Volmer constant (KD) was determined as the slope of the strait of the modified Stern–Volmer equation $\frac{F0}{F} = 1 + k_q\tau[Q] = 1 + KD[DOX]$. The value of k_q was calculated as KD/τ (τ for static quenching of HSA = 5.9 ns) (Agudelo 2012), K_d was calculated as $1/_{KD}$.

To determine the *n* value of DOX to HSA, the $\log_{10}$(F0-F) was plotted versus $\log_{10}$ of quencher molar concentration. After linear regression, the *n* value was determined as the slope of the straight from the equation $\log \frac{F0-F}{F} = \log 1/K_d + n \log[DOX]$.

To assess the K_d, k_q, and *n* values of HSA–DOX interaction when albumin was bonded on MelaSil_Ag-HSA NPs, the same experimental setup used for free HSA was exploited, by using the MelaSil_Ag-HSA NPs corresponding to HSA 10 μM.

3.5 Evaluation of HSA amount bonded to MelaSil_Ag NPs

The amount of HSA bonded to NPs was determined by measuring the unbonded HSA after the functionalization process (Sanità 2020a). Unbonded HSA was precipitated through trichloroacetic acid (TCA) solution from every supernatant during the HSA functionalization protocol. The HSA precipitation was carried out by adding 10% v/v volume of TCA 100% to the supernatants. After 30' at 4°C, the precipitate was collected by centrifugation at 12,000 × g for 30' at 4°C, dried at 80°C overnight (ON), and weighted with an analytical balance. The amount of HSA linked to MelaSil_Ag NPs was calculated as the subtraction of the unbonded albumin to the total amount used in the functionalization process. The percentage of HSA bonded to MelaSil_Ag NPs was obtained as (mg of bonded HSA/mg of MelaSil_Ag NPs) × 100.

3.6 Loading of DOX to MelaSil_Ag-HSA NPs

To load DOX on HSA modified NPs, MelaSil_Ag-HSA NPs (2.6 mg/mL) were added to DOX (with HSA:DOX ratio of 1:40) in PBS 1× for 96h under stirring (24h at RT and 72h at 4°C). Next, DOX-loaded NPs were collected by centrifugation and washed 3 times with PBS 1×. To calculate the DOX amount bonded to HSA-NPs, a fluorescence calibration curve (Ex: 480 nm, Em: 590 nm) measured with a Multilabel Reader (PerkinElmer, Waltham, MA, USA) was used. The bonded DOX was obtained by subtracting the unbonded DOX from the total amount used. The DOX bond efficiency and capacity was calculated as (mg of bonded DOX/mg of total DOX) × 100 and (mg of bonded DOX/mg of MelaSil_Ag-HSA NPs) × 100, respectively.

3.7 Dynamic light scattering and ζ-potential characterization

Size distributions and ζ-potentials of MelaSil_Ag, MelaSil_Ag-HSA, and MelaSil_Ag-HSA@DOX NPs were measured by a Zetasizer (Nanoseries, Malvern) using the laser dynamic scattering (λ = 632.8 nm) and the particle electrophoresis techniques, respectively. All the samples were diluted up to a droplet concentration of approximately 0.025% w/v by using Milli-Q water. A detecting angle of 173° and 5 runs for each measurement (1 run lasting 100 s) were used in the calculations of the particle size distribution. ζ-potential analyses were carried out by setting 50 runs for each measurement.

3.8 DOX release from MelaSil_Ag-HSA@DOX NPs

To evaluate the DOX release from loaded NPs at two different pH levels (5.2 and 7.4), MelaSil_Ag-HSA@DOX NPs were incubated at 2.6 mg/mL in PBS 1× at 37°C under stirring for 0.5, 4, 24, and 48h. Successively, the NPs were collected by centrifugation and the amount of released DOX was calculated by using a Multilabel Reader. The amount of DOX released by MelaSil_Ag-HSA@DOX NPs was plotted as percentage of the total amount of DOX bonded to NPs.

3.9 Confocal microscopy of 2D cells

HS578T cells (5×10^3/coverslip) were plated on 10 mm glass coverslips positioned on the bottom of 24-well plate, allowed to attach for 24h under normal cell culture conditions and then incubated with MelaSil_Ag-HSA@DOX NPs at 120 µg/mL (corresponding to 2.6 µM of DOX) for 3 and 6h at 37°C. Cells were washed with PBS, fixed in 4% formaldehyde for 20 min, and washed 3 times with PBS. Cell nuclei were then stained with Hoechst 33258 (Invitrogen, Carlsbad, CA, USA). Cells were then spotted on microscope slides and analyzed. Experiments were carried out on an inverted and motorized microscope (Axio Observer Z.1) equipped with a 63×/1.4 Plan Apochromat objective. The attached laser scanning unit (LSM 700 4× pigtailed laser 405–488–555–639; Zeiss, Jena, Germany) enabled confocal imaging. For excitation, 405 nm and 480 nm lasers were used. Fluorescence emission was revealed by Main Dichroic Beam Splitter and Variable Secondary Dichroic Beam Splitter. Double staining fluorescence images were acquired separately using ZEN 2012 software in the red and blue channels at a resolution of 512 × 512 pixels, with the confocal pinhole set to one Airy unit, and then saved in TIFF format.

3.10 Cell viability assays

To evaluate MelaSil_Ag-HSA@DOX NPs toxicity, CellTiter-GLO assay and Live Cell Explorer assay, according to the manufacturer's instructions, were used. Luminescence was recorded for 0.25 s per well by a Multilabel Reader, while images were acquired by using a digital camera (Panasonic Lumix DC-FZ82 Bridge) with a 10x magnification.

For CellTiter-GLO assay, HS578T cells were seeded into 96 opaque-walled plates at the density of 5×10^3 cells/well and incubated with free DOX at 0.65, 1.3 and 2.6 µM and MelaSil_Ag-HSA@DOX NPs were used at a concentration depending on the DOX loading efficiency and corresponding to the same DOX concentration (NPs ≅ 30, 60 and 120 µg/mL). The assay was performed after 24, 48, and 72h of incubation for HS578T cells. For MCF10a cells, CellTiter-GLO assay was performed by using 1.3 and 2.6 µM of DOX carried by MelaSil_Ag-HSA@DOX NPs, for 24 and 48h.

For Live Cell Explorer assay, HS578T cells were seeded into 24-well microtiter plates at the density of 40×10^3 cells/well and incubated with free DOX and MelaSil_Ag-HSA@DOX NPs in the same experimental conditions. After

incubation, cells were observed by fluorescence microscopy and images were acquired.

3.11 Photothermal response of MelaSil_Ag NPs under CW laser irradiation

The thermal behavior of MelaSil_Ag NPs was studied under prolonged laser illumination at 808 nm continuous wavelength (CW), a custom-made setup. In detail, 500 μL of NPs (1 μg/μL) were loaded in a polystyrene cuvette, then placed inside a cuvette holder, in which, on the left side was an optical fiber for laser illumination and on the right side was a power meter to measure the outgoing laser irradiation. The thermal infrared images were acquired during the NP heating (15 min) and cooling (10 min) steps, at a 10 Hz rate in matrices of 60 × 84 pixels, recording in time the absorbed power.

3.12 Cell viability following laser irradiation

For the PT experiments, HS578T cells were seeded into white 96-well plates at the density of 2×10^3 cells/well. Then, cells were incubated with MelaSil_Ag-HSA@DOX NPs or MelaSil_Ag-HSA NPs for 3, 6 or 16h. MelaSil_Ag-HSA@DOX NPs were used at a concentration corresponding to 0.65, 1.3 and 2.6 μM of DOX; MelaSil_Ag-HSA NPs were used at the same concentrations of MelaSil_Ag-HSA@DOX NPs. At the end of the incubation time, the medium was replaced with fresh medium and the cells were irradiated at 808 nm CW laser for 5 min, with a mean power density of 3 W/cm^2. During irradiation, cells were maintained at 37°C. Cell viability was assessed 24h after irradiation by the CellTiter-GLO assay, as described above.

4. Results

4.1 Evaluation of MelaSil_Ag-HSA@DOX NPs cytotoxicity in 2D and 3D models

4.1.1 Doxorubicin and human serum albumin interaction

A preliminary analysis of the DOX-HSA interaction was carried out. To evaluate the DOX–HSA interaction, HSA at 10 µM was incubated with DOX at increasing concentrations (from 0 to 400 µM). The HSA fluorescence spectra (Ex 280 nm) were recorded from 287 to 500 nm for each DOX concentration (Figure 16A). This preliminary result show that a good bonding capability was at 400 µM of DOX, in a molar ratio HSA:DOX of 1:40. Then, the number of binding sites (*n*), the quenching constant (k_q) and the dissociation constant (K_d) and relative quenching parameters through a Stern–Volmer plot were established. The *n* value, for each HSA molecule, determined by $\log_{10}$ ($\frac{F0-F}{F}$) versus $\log_{10}$ of quencher molar concentration, was 1.5, according with literature (Figure 16B) (Agudelo 2012). Moreover, the quenching constant (k_q = 0.96 x 10^{12}), which acts as a measure of quenching efficiency, indicates that the quenching process shows a good efficiency (Figure 16C), and the value of K_d (177 µM), an index of the quenching efficiency, suggests a strong interaction between fluorophore and quencher.

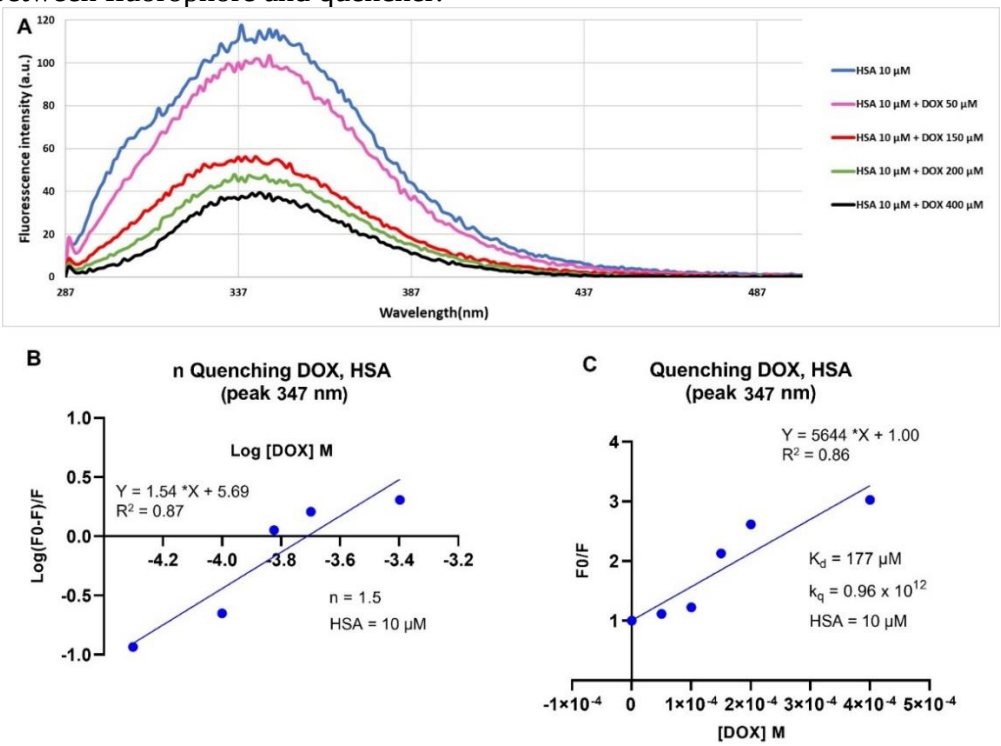

Figure 16: Fluorescence emission spectra and Stern–Volmer plots for HSA–doxorubicin interaction. **A**) Fluorescence emission spectra; **B**) Stern–Volmer plot of HSA binding sites; **C**) Stern–Volmer plot of K_d and k_q. $p < 0.05$.

4.1.2 DOX and MelaSil_Ag-HSA nanoparticles interaction

The interaction between DOX and HSA bonded to MelaSil_Ag NPs was evaluated by recording the fluorescence spectra of MelaSil_Ag-HSA NPs (HSA 10 µM) with and without DOX at increasing concentrations (Figure 17A).
The spectra were collected by using the same experimental conditions previously used. The fluorescence spectra showed a quenching effect clearly visible up to 400 µM of DOX (Figure 17B) and the Stern-Volmer formula was used to obtain the kinetic parameters (n = 1.6, k_q= 29.26 x 10^{12} and K_d = 56 µM) (Figure 17C and 17D).

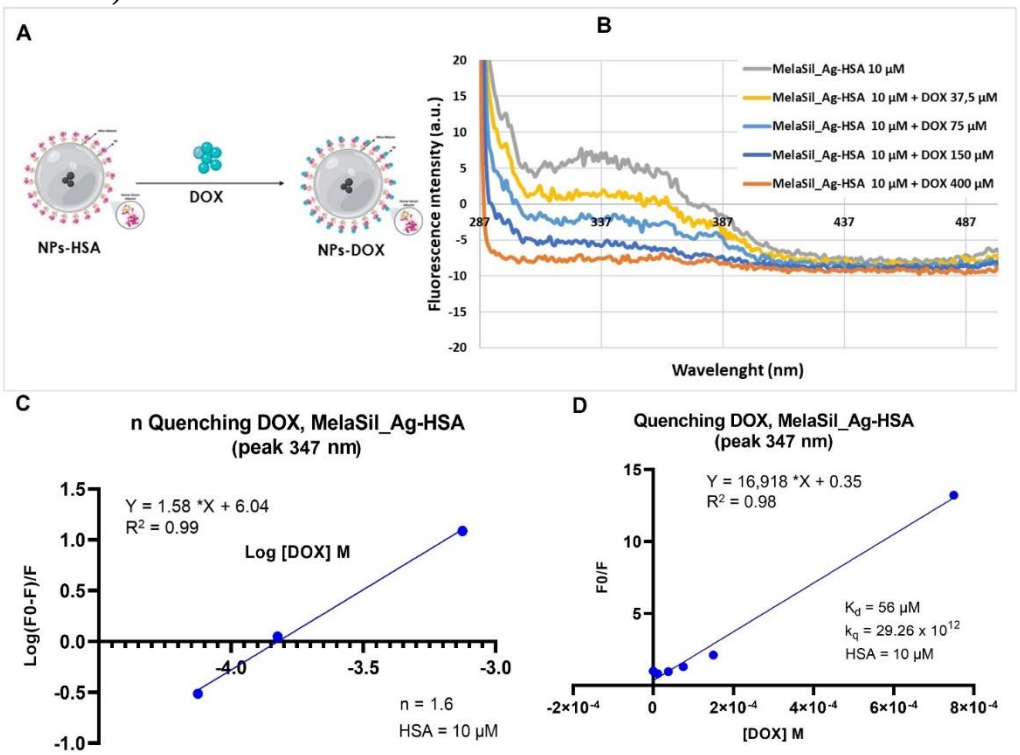

Figure 17: Fluorescence emission spectra and Stern–Volmer plots for MelaSil_Ag-HSA NPs–doxorubicin interaction. **A**) DOX loading scheme; **B**) Fluorescence emission spectra; **C**) Stern–Volmer plot of HSA binding sites; **D**) Stern–Volmer plot of K_d and k_q. $p < 0.05$.

4.1.3 Drug loading on MelaSil_Ag-HSA NPs

The intrinsic fluorescence of DOX was used to calculate the amount of DOX loaded on MelaSil_Ag-HSA NPs, as reported in "Materials and Methods" section. For each MelaSil_Ag-HSA@DOX NPs preparation, the DOX bond efficiency and capacity were calculated and, on average, the DOX concentration was approximately 0.02 μM per 1 μg/mL of NPs. Then, hydrodynamic diameter, polydispersity index (PDI), and ζ-potential both before and after drug loading were evaluated, showing a slight increase in size of DOX@NPs up to 407 nm ± 29 nm (PDI 0.45) with a ζ-potential of -17 ± 2.16 mV, as shown in Table 2 (Figure 18).

Table 2: DLS and ζ-potential of MelaSil_Ag-HSA NPs before and after DOX conjugation.

	ζ -average (nm)	**PDI**	**ζ-Potential (mV)**
MelaSil_Ag-HSA NPs	394 ± 32	0.26 ± 0.9	- 27.2 ± 1.65
MelaSil_Ag-HSA@DOX NPs	407 ± 29	0.45 ± 0.09	- 17 ± 2.16

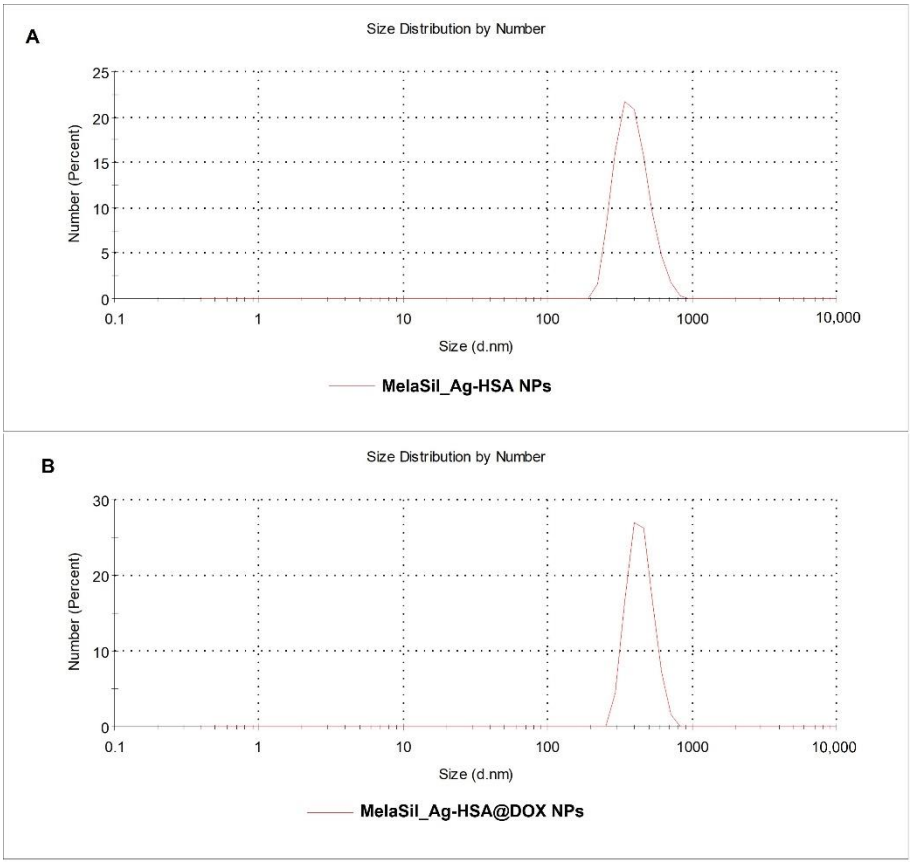

Figure 18: Number distribution (%) of DLS measurements on **A**) MelaSil_Ag-HSA NPs at 100 μg/mL and **B**) MelaSil_Ag-HSA@DOX NPs at 100 μg/mL.

4.1.4 Drug release

The DOX release profile was assessed *in vitro* up to 48h of incubation at acidic pH (pH 5.2) and physiological pH (pH 7.4). At acidic pH, 50% of the drug was released in the first 30 minutes and up to 80% after 24h, followed by a slow and sustained release. Contrary, at physiological pH, a maximum drug release of about 20% after 30 minutes was observed, this value remained constant up to 48h. (Figure 19).

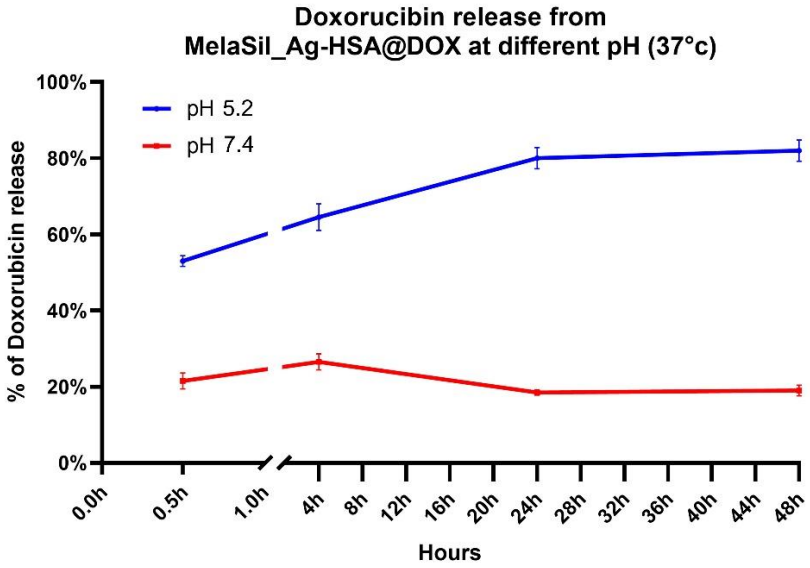

Figure 19: Doxorubicin release at pH 5.2 and pH 7.4. $p < 0.05$.

4.1.5 DOX delivery in breast cancer cells

To evaluate nuclear localization of the drug delivered by MelaSil_Ag-HSA@DOX NPs, confocal microscopy was performed. HS578T cells were treated with DOX@NPs with an amount of DOX of about 2.6 μM (NPs = 120 μg/mL) at 37°C for 3 and 6h. The images reveal a significant degree of internalization inside cell nuclei, indicating a good DOX delivery into cells (Figure 20).

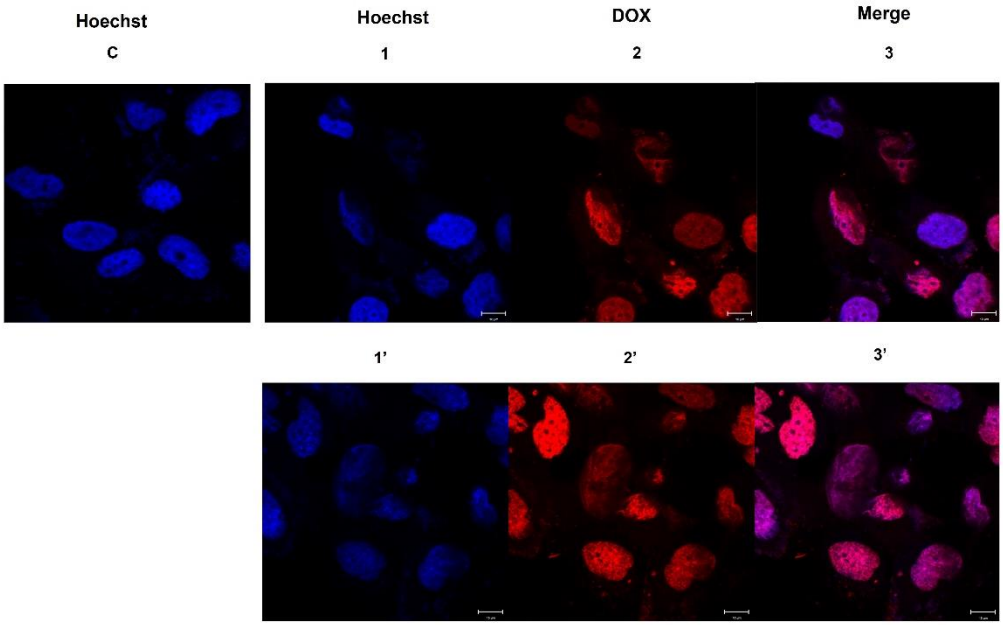

Figure 20: Representative images of confocal microscopy analysis of HS578T cells treated with HSA@DOX NPs. **C**) Control; **1–3**) MelaSil_Ag-HSA@DOX NPs 3h; **1'–3'**) MelaSil_Ag-HSA@DOX NPs 6h. Cell nuclei were stained with Hoechst 33258; DOX is visible as red color. Scale bar: 10 μm.

4.1.6 Cytotoxicity of MelaSil_Ag-HSA@DOX NPs vs. free DOX in 2D cells

CellTiter-GLO and Live Cell Explorer assays were used to assess the cytotoxicity of MelaSil_Ag-HSA@DOX NPs compared to free DOX. For CellTiter-GLO assay, HS578T breast cancer cells were cultured for 24, 48, and 72h with increasing concentrations of DOX-loaded NPs (30, 60, and 120 μg/mL with an amount of DOX of about 0.65, 1.3, and 2.6 μM, respectively) and the corresponding concentrations of free DOX. Results show a viability decrease of 40% and 67% after 24h of incubation at a concentration of DOX delivered by NPs of 1.3 and 2.6 μM, respectively, versus 20% and 39% with the same concentrations of free DOX. After 48h, a toxicity of 73% (DOX@NPs) vs. 48% (free DOX) was observed. At prolonged incubation time (72h), the DOX carried by NPs at 0.65 μM showed a high toxic effect (53%) compared to the free DOX (13%) (Figure 21A). Furthermore, to evaluate toxicity in healthy cells, MCF10a (mammary breast fibrocystic disease cells) were incubated with DOX@NPs with an amount of drug of 1.3 and 2.6 μM and the results show a significant lower toxicity in healthy cells compared to breast cancer cells. After 48h of incubation MCF10a showed of 61% of vitality versus 16% of HS578T (Figure 21B). For Live Cell Explorer assay, HS578T cells were treated at increasing incubation time with free DOX (1.3 μM) and MelaSil_Ag-HSA@DOX NPs (60 μg/mL with DOX at 1.3 μM) (Figure 21C). According with CellTiter-GLO assay, in all tested conditions, DOX carried by NPs is more toxic than free drug.

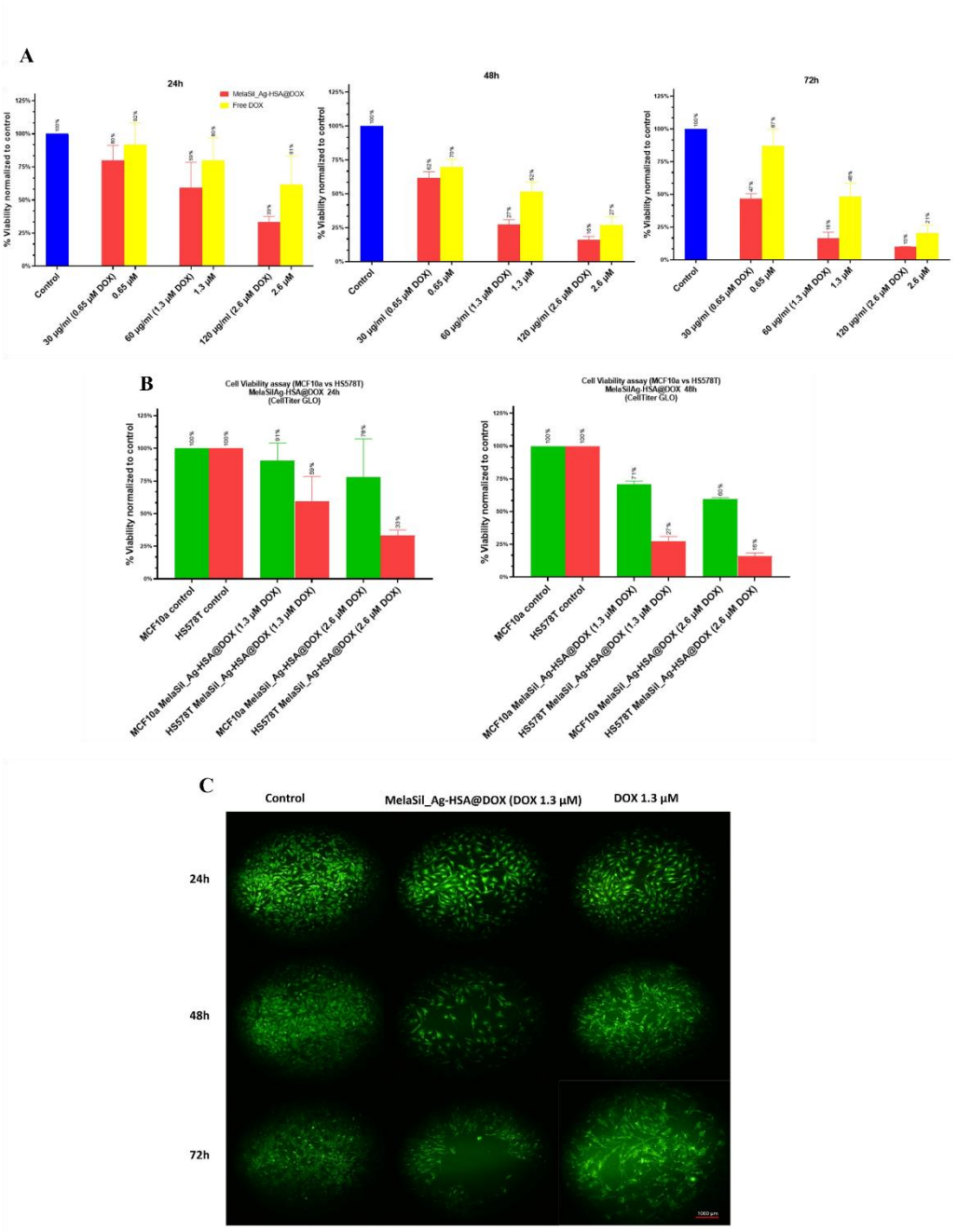

Figure 21: Cell viability assays. **A**) CellTiter-GLO assay of HS578T cells treated for 24, 48, and 72h with MelaSil_Ag-HSA@DOX NPs (30, 60 and 120 µg/mL corresponded to DOX 0.65, 1.3 and 2.6 µM) and free DOX (at the same concentrations). $p < 0.05$; **B**) Cell-Titer GLO assay of HS578T and MCF10a cell lines treated for 24 and 48h with MelaSil_Ag-HSA@DOX NPs. $p < 0.05$; **C**) Representative images of Calcein-AM fluorescent morphology images of HS578T cells before and after treatment with MelaSil_Ag-HSA@DOX NPs and free DOX. Scale bar: 1000 µm.

4.1.7 Thermal properties of MelaSil_Ag-HSA NPs

By using spectrophotometric analysis, the light absorbance characteristics of the MelaSil_Ag-HSA NPs were examined (Figure 22A and 22B). MelaSil_Ag-HSA NPs have an absorbance value of approximately 0.69 at 808 nm wavelength and they display a temperature increase of 14 °C (from 25 to 39 °C) after 15 minutes of laser irradiation (Figure 22C). The heating behavior was fitted according to a second-order exponential curve (f1):

$$\Delta T = a*e^{(b*t)} + c*e^{(d*t)} \quad (f1)$$

and, after continuous wavelength laser stimulation, NPs show a temperature increase up to 10 °C in about 200 s, as shown in Figure 22D.

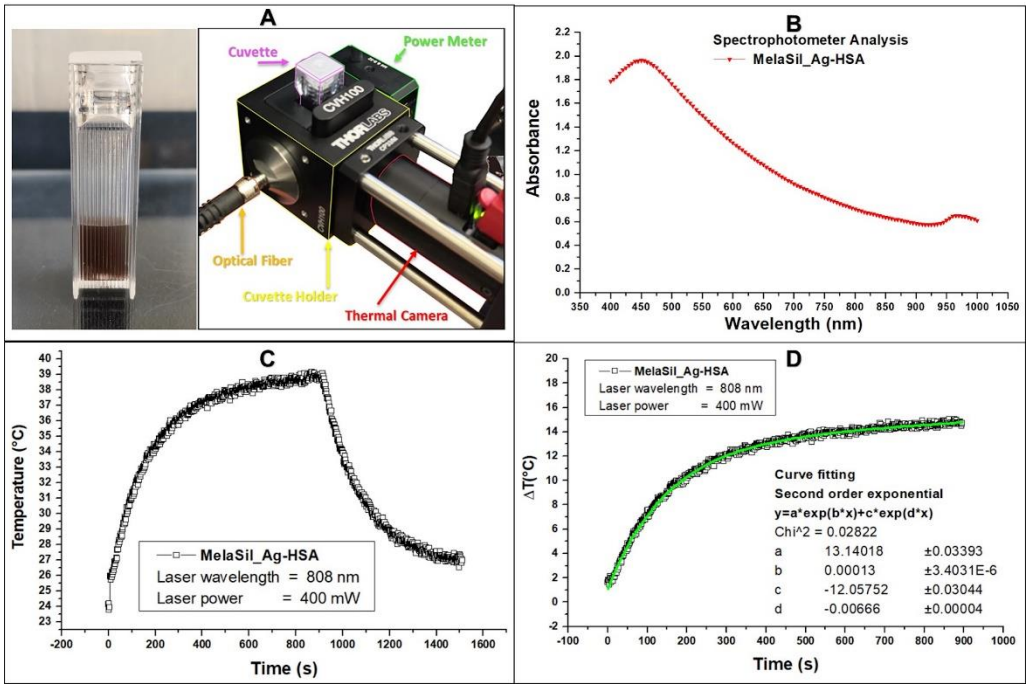

Figure 22: Thermal properties of MelaSil_Ag−HSA NPS. **A**) MelaSil_Ag−HSA NPs (1 µg/µL); **B**) spectrophotometric analysis of the light absorbance properties of MelaSil_Ag−HSA NPs; **C**) typical thermal trends of MelaSil_Ag-HSA NPs, CW heating (laser on), and cooling (laser off) processes; **D**) dynamic evaluation of heating performances of MelaSil_Ag−HSA NPs during laser illumination, and the fitting curve (green) of ΔT vs. time.

4.1.8 Thermal trend of DMEM and DOX

Thermal trend of DMEM culture medium as a function of 808 nm laser irradiation time was evaluated and no significant change in presence or in absence of the light was observed (Figure 23A). Furthermore, the spectrophotometric analysis of the light absorbance properties at a wavelength of 808 nm of free DOX (100 µM) in DMEM and free DOX (100 µM) in PBS was performed. As reported in Figure 23B, results show no significant DOX absorbance at 808 nm.

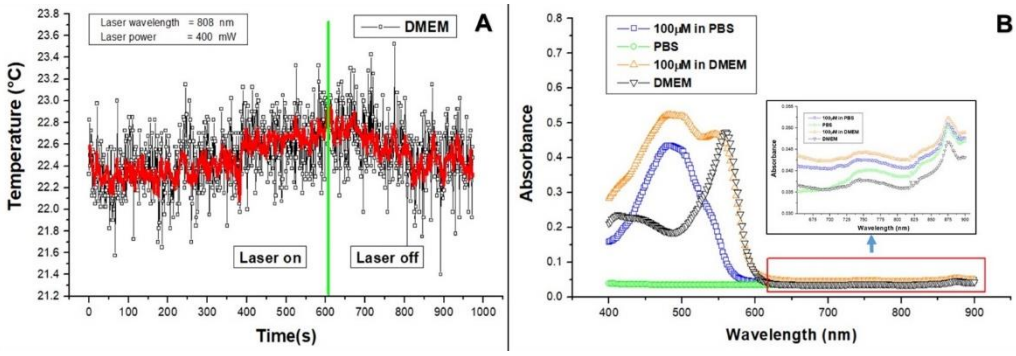

Figure 23: A) Thermal trend of DMEM culture medium as a function of 808 nm laser irradiation (400 mW) time. CW heating (laser on) and cooling (laser off) processes. **B**) Spectrophotometric analysis of the light absorbance properties of free DOX (100 µM) in DMEM (orange) and free DOX (100 µM) in PBS (blue), DMEM (black) and PBS (green)**.**

4.1.9 Cytotoxicity of MelaSil_Ag-HSA@DOX upon laser irradiation

To evaluate the cytotoxicity of MelaSil_Ag-HSA@DOX NPs upon laser irradiation, HS578T cells were incubated for 3, 6 and 16h with increasing concentrations of MelaSil_Ag-HSA@DOX NPs (30, 60 and 120 μg/mL with an amount of DOX of 0.65 , 1.3 and 2.6 μM, respectively) and exposed to laser photothermal irradiation (3 W/cm^2) for 5 minutes (Figure 24).
After 3h of incubation, a dose-dependent reduction in cell viability was observed for MelaSil_Ag-HSA@DOX NPs in comparison to MelaSil_Ag-HSA NPs at the same concentrations (51.3%, 75.0%, and 79.9% at 0.65, 1.3 and 2.6μM DOX vs. 7.5%, 49.6%, and 58.4% at 30, 60 and 120 μg/mL, respectively). After 6h of incubation, DOX-loaded NPs (0.65 μM of DOX) caused a dramatic decrease of cell viability compared to HSA-NPs (80.2% vs. 8.4%, respectively). After 16h of incubation, a rise of PTT efficacy was observed for MelaSil_Ag-HSA NPs, but MelaSil_Ag-HSA@DOX NPs (0.65 μM of DOX) generated a greater cytotoxic effect (61.2% vs 92.2%, respectively).

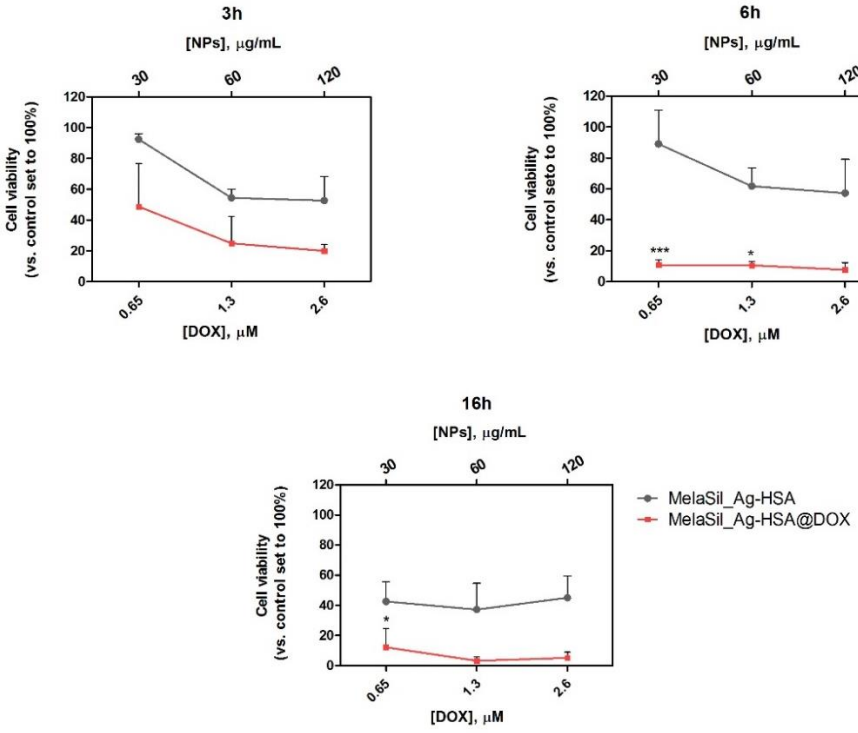

Figure 24: Cell viability of HS578T following 808 nm CW laser irradiation. Cells treated for 3, 6, and 16h with MelaSil_Ag-HSA@DOX NPs (red) or MelaSil_Ag-HSA NPs (gray) at the concentrations of 30, 60, and 120 μg/mL (upper X axis), corresponding to 0.65, 1.3, and 2.6 μM DOX, respectively, for DOX-loaded NPs (lower X axis) and irradiated for 5'. * $p < 0.05$ and *** $p < 0.001$ versus cells treated with MelaSil_Ag-HSA NPs. CellTiter-GLO assay was performed 24h after irradiation.

7. Acknowledgements

8. List of publications

Ruthenium complexes effects on cancer cell growth.
In preparation.

Photoacoustic imaging and chemo- photothermal therapy of solid tumors: 3D spheroids as a predictive model for nanotheranostics.
In preparation.

Nanoparticles design for theranostic approach in cancer disease.
Cancers [2022]
https://doi.org/10.3390/cancers14194654
Barbara Carrese, Gennaro Sanità and Annalisa Lamberti.

Controlled Release of Doxorubicin for Targeted Chemo-Photothermal Therapy in Breast Cancer HS578T Cells using Albumin Modified Hybrid Nanocarriers.
Int. J. Mol. Sci. [2021]
https://doi.org/ 10.3390/ijms222011228
Barbara Carrese, Chiara Cavallini, Gennaro Sanità, Paolo Armanetti, Brigida Silvestri, Gaetano Calì, Giulio, Giuseppina Luciani, Luca Menichetti, Annalisa Lamberti.

Albumin-Modified Melanin-Silica hybrid nanoparticles target breast cancer cells via a SPARC-Dependent mechanism.
Front. Bioeng. Biotechnol. [2020]
http://doi.org/10.3389/fbioe.2020.00765
Gennaro Sanità, Paolo Armanetti, Brigida Silvestri, **Barbara Carrese**, Gaetano Calì, Giulio Pota, Alessandro Pezzella, Marco D'Ischia, Giuseppina Luciani, Luca Menichetti, Annalisa Lamberti.

Nanoparticle surface functionalization: how to improve biocompatibility and cellular internalization.
Front. Mol. Biosci. [2020]
https://doi.org/10.3389/fmolb.2020.587012
Gennaro Sanità, **Barbara Carrese**, Annalisa Lamberti.

9. References

Abadeer N.S., Murphy C.J., 2021. Recent progress in cancer thermal therapy using gold nanoparticles. Nanomaterials and Neoplasms 143–217.

Aghda N.H., Abdulsahib S.M., Severson C., Lara E.J., Hurtado S.T., Yildiz T., Castillo J.A., Tunnell J.W., Betancourt T., 2020. Induction of immunogenic cell death of cancer cells through nanoparticle-mediated dual chemotherapy and photothermal therapy. Int J Pharm 589, 119787.

Agudelo D., Bourassa,ì P., Bruneau J., Berube G., Asselin E., Tajmir-Riahi H.-A., 2012. Probing the binding sites of antibiotic drugs doxorubicin and N-(trifluoroacetyl) doxorubicin with human and bovine serum albumins.

An F., Yang Z., Zheng M., Mei T., Deng G., Guo P., Li Y., Sheng R., 2020. Rationally assembled albumin/indocyanine green nanocomplex for enhanced tumor imaging to guide photothermal therapy. J Nanobiotechnology 18, 1–11.

An F.-F., Zhang X.-H., 2017. Strategies for preparing albumin-based nanoparticles for multifunctional bioimaging and drug delivery. Theranostics 7, 3667.

Arshad R., Kiani M.H., Rahdar A., Sargazi S., Barani M., Shojaei S., Bilal M., Kumar D., Pandey S., 2022. Nano-Based Theranostic Platforms for Breast Cancer: A Review of Latest Advancements. Bioengineering 9, 320.

Awan U.A., Raza A., Ali S., Saeed R.F., Akhtar N., 2021. Doxorubicin-loaded gold nanorods: a multifunctional chemo-photothermal nanoplatform for cancer management. Beilstein Journal of Nanotechnology 12, 295–303.

Bairagi U., Mittal P., Mishra B., 2015. Albumin: a versatile drug carrier. Austin Therapeutics 2, 1021.

Bazak R., Houri M., el Achy S., Hussein W., Refaat T., 2014. Passive targeting of nanoparticles to cancer: A comprehensive review of the literature. Mol Clin Oncol 2, 904–908.

Bhushan B., Khanadeev V., Khlebtsov B., Khlebtsov N., Gopinath P., 2017. Impact of albumin based approaches in nanomedicine: Imaging, targeting and drug delivery. Adv Colloid Interface Sci 246, 13–39.

Białkowska K., Komorowski P., Bryszewska M., Miłowska K., 2020. Spheroids as a type of three-dimensional cell cultures—examples of methods of preparation and the most important application. Int J Mol Sci 21, 6225.

Buzea C., Pacheco I.I., Robbie K., 2007. Nanomaterials and nanoparticles: sources and toxicity. Biointerphases 2, MR17–MR71.

Carrese B., Cavallini C., Sanità G., Armanetti P., Silvestri B., Calì G., Pota G., Luciani G., Menichetti L., Lamberti A., 2021. Controlled Release of Doxorubicin for Targeted Chemo-Photothermal Therapy in Breast Cancer HS578T Cells Using Albumin Modified Hybrid Nanocarriers. Int J Mol Sci 22, 11228.

Carrese B., Sanità G., Lamberti A., 2022. Nanoparticles Design for Theranostic Approach in Cancer Disease. Cancers (Basel) 14, 4654.

Cartabellotta A., Laganà A.S., Leoni M., Quintaliani G., Zampieri P., Potena A., 2017. La diagnosi precoce dei tumori.

Chattopadhyay D., 2022. Cisplatin. Resonance 27, 659–666.

Chen Y., Feng X., Yuan Y., Jiang J., Zhang P., Zhang B., 2022. Identification of a novel mechanism for reversal of doxorubicin-induced chemotherapy resistance by TXNIP in triple-negative breast cancer via promoting reactive oxygen-mediated DNA damage. Cell Death Dis 13, 1–13.

Chlenski A., Dobratic M., Salwen H.R., Applebaum M., Guerrero L.J., Miller R., DeWane G., Solomaha E., Marks J.D., Cohn S.L., 2016. Secreted protein acidic and rich in cysteine (SPARC) induces lipotoxicity in neuroblastoma by regulating transport of albumin complexed with fatty acids. Oncotarget 7, 77696.

Chow J.C.L., 2022. Application of Nanomaterials in Biomedical Imaging and Cancer Therapy. Nanomaterials 12, 726.

Cleator S., Heller W., Coombes R.C., 2007. Triple-negative breast cancer: therapeutic options. Lancet Oncol 8, 235–244.

Cortes J., Saura C., 2010. Nanoparticle albumin-bound (nabTM)-paclitaxel: improving efficacy and tolerability by targeted drug delivery in metastatic breast cancer. European Journal of Cancer Supplements 8, 1–10.

Costa C.O., Neto J.H.A., Baliza I.R.S., Dias R.B., Valverde L. de F., Vidal M.T.A., Sales C.B.S., Rocha C.A.G., Moreira D.R.M., Soares M.B.P., 2017. Novel piplartine-containing ruthenium complexes: synthesis, cell growth inhibition, apoptosis induction and ROS production on HCT116 cells. Oncotarget 8, 104367.

Dasari S., Njiki S., Mbemi A., Yedjou C.G., Tchounwou P.B., 2022. Pharmacological effects of cisplatin combination with natural products in cancer chemotherapy. Int J Mol Sci 23, 1532.

Desai N., Trieu V., Damascelli B., Soon-Shiong P., 2009. SPARC expression correlates with tumor response to albumin-bound paclitaxel in head and neck cancer patients. Transl Oncol 2, 59–64.

Du Q., Qi X., Zhang M., Zhao Z., Li Q., Ren X., Wang N., Luan Y., 2021. A mitochondrial-metabolism-regulatable carrier-free nanodrug to amplify the sensitivity of photothermal therapy. Chemical Communications 57, 8993–8996.

Egea J., López-Muñoz F., Fernández-Capetillo O., Reiter R.J., Romero A., 2022. Alkylating Agent-Induced Toxicity and Melatonin-Based Therapies. Front Pharmacol 13, 873197.

Ferlay J., Colombet M., Soerjomataram I., Parkin D.M., Piñeros M., Znaor A., Bray, F., 2021. Cancer statistics for the year 2020: An overview. Int J Cancer 149, 778–789.

Fetoni A.R., Paciello F., Troiani D., 2022. Cisplatin Chemotherapy and Cochlear Damage: Otoprotective and Chemosensitization Properties of Polyphenols. Antioxid Redox Signal 36, 1229–1245.

Foulkes W.D., Smith I.E., Reis-Filho J.S., 2010. Triple-negative breast cancer. New England journal of medicine 363, 1938–1948.

Fu D., Calvo J.A., Samson L.D., 2012. Balancing repair and tolerance of DNA damage caused by alkylating agents. Nat Rev Cancer 12, 104–120.

Gatoo M.A., Naseem S., Arfat M.Y., Mahmood Dar A., Qasim K., Zubair S., 2014. Physicochemical properties of nanomaterials: implication in associated toxic manifestations. Biomed Res Int 2014.

Gilson R. C., Black K. C., Lane D. D., Achilefu S. (2017). Hybrid TiO2–Ruthenium Nano-photosensitizer Synergistically Produces Reactive Oxygen Species in both Hypoxic and Normoxic Conditions. Angewandte Chemie, 129(36), 10857-10860.

Greish K., 2010. Enhanced permeability and retention (EPR) effect for anticancer nanomedicine drug targeting, in: Cancer Nanotechnology. Springer, pp. 25–37.

Hamilton G., Rath B., 2019. Applicability of tumor spheroids for in vitro chemosensitivity assays. Expert Opin Drug Metab Toxicol 15, 15–23.

He L., Huang Y., Zhu H., Pang G., Zheng W., Wong Y., Chen T., 2014. Cancer-Targeted Monodisperse Mesoporous Silica Nanoparticles as Carrier of Ruthenium Polypyridyl Complexes to Enhance Theranostic Effects. Adv Funct Mater 24, 2754–2763.

He Q., Gao Y., Zhang L., Zhang Z., Gao F., Ji X., Li Y., Shi J., 2011. A pH-responsive mesoporous silica nanoparticles-based multi-drug delivery system for overcoming multi-drug resistance. Biomaterials 32, 7711–7720.

He X.M., Carter D.C., 1992. Atomic structure and chemistry of human serum albumin. Nature 358, 209–215.

Henrique R.B.L., Lima R.R.M., Monteiro C.A.P., Oliveira W.F., Pereira G., Cabral Filho P.E., Fontes A., 2022. Advances in the study of spheroids as versatile models to evaluate biological interactions of inorganic nanoparticles. Life Sci 120657.

Hoang B., Ernsting M.J., Roy A., Murakami M., Undzys E., Li S.-D., 2015. Docetaxel-carboxymethylcellulose nanoparticles target cells via a SPARC and albumin dependent mechanism. Biomaterials 59, 66–76.

Huang Y., Lai H., Jiang J., Xu X., Zeng Z., Ren L., Liu Q., Chen M., Zhang T., Ding X., 2022. pH-activatable oxidative stress amplifying dissolving microneedles for combined chemo-photodynamic therapy of melanoma. Asian J Pharm Sci.

Iravani S., Varma R.S., 2022. MXenes in cancer nanotheranostics. Nanomaterials 12, 3360.

Irvin Jr W.J., Carey L.A., 2008. What is triple-negative breast cancer? Eur J Cancer 44, 2799–2805.

Jafari S.H., Saadatpour Z., Salmaninejad A., Momeni F., Mokhtari M., Nahand J.S., Rahmati M., Mirzaei H., Kianmehr M., 2018. Breast cancer diagnosis: Imaging techniques and biochemical markers. J Cell Physiol 233, 5200–5213.

Jiang G.-B., Zhang W.-Y., He M., Gu Y.-Y., Bai L., Wang Y.-J., Yi Q.-Y., Du F., 2020. New ruthenium polypyridyl complexes functionalized with fluorine atom or furan: Synthesis, DNA-binding, cytotoxicity and antitumor mechanism studies. Spectrochim Acta A Mol Biomol Spectrosc 227, 117534.

Kievit F.M., Zhang M., 2011. Cancer nanotheranostics: improving imaging and therapy by targeted delivery across biological barriers. Advanced materials 23, H217–H247.

Knežević N.Ž., Stojanovic V., Chaix A., Bouffard E., el Cheikh K., Morère A., Maynadier M., Lemercier G., Garcia M., Gary-Bobo M., 2016. Ruthenium (ii) complex-photosensitized multifunctionalized porous silicon nanoparticles for two-photon near-infrared light responsive imaging and photodynamic cancer therapy. J Mater Chem B 4, 1337–1342.

Konda P., Roque III J.A., Lifshits L.M., Alcos A., Azzam E., Shi G., Cameron C.G., McFarland S.A., Gujar S., 2022. Photodynamic therapy of melanoma with new, structurally similar, NIR-absorbing ruthenium (II) complexes promotes

tumor growth control via distinct hallmarks of immunogenic cell death. Am J Cancer Res 12, 210.

Kratz F., 2008. Albumin as a drug carrier: design of prodrugs, drug conjugates and nanoparticles. Journal of controlled release 132, 171–183.

Lammers T., Aime S., Hennink W.E., Storm G., Kiessling F., 2011. Theranostic nanomedicine. Acc Chem Res 44, 1029–1038.

Larsen M.T., Kuhlmann M., Hvam M.L., Howard K.A., 2016. Albumin-based drug delivery: harnessing nature to cure disease. Mol Cell Ther 4, 1–12.

Lee S.Y., Kim C.Y., Nam T.-G., 2020. Ruthenium complexes as anticancer agents: A brief history and perspectives. Drug Des Devel Ther 14, 5375.

Li J., Chen T., 2020. Transition metal complexes as photosensitizers for integrated cancer theranostic applications. Coord Chem Rev 418, 213355.

Lifshits L.M., Roque III J.A., Konda P., Monro S., Cole H.D., von Dohlen D., Kim S., Deep G., Thummel R.P., Cameron C.G., 2020. Near-infrared absorbing Ru (II) complexes act as immunoprotective photodynamic therapy (PDT) agents against aggressive melanoma. Chem Sci 11, 11740–11762.

Lippert B., editor, 1999. Chemistry and biochemistry of a leading anticancer drug. Verlag Helvetica Chimica Acta, Zürich.

Liu J., Lai H., Xiong Z., Chen B., Chen T., 2019. Functionalization and cancer-targeting design of ruthenium complexes for precise cancer therapy. Chemical Communications 55, 9904–9914.

Liu X., Geng P., Yu N., Xie Z., Feng Y., Jiang Q., Li M., Song Y., Lian W., Chen Z., 2022. Multifunctional Doxorubicin@ Hollow-Cu9S8 nanoplatforms for Photothermally-Augmented Chemodynamic-Chemo therapy. J Colloid Interface Sci 615, 38–49.

Liu Z., Chen X., 2016. Simple bioconjugate chemistry serves great clinical advances: albumin as a versatile platform for diagnosis and precision therapy. Chem Soc Rev 45, 1432–1456.

Lopes J., Rodrigues C.M.P., Gaspar M.M., Reis C.P., 2022. How to Treat Melanoma? The Current Status of Innovative Nanotechnological Strategies and the Role of Minimally Invasive Approaches like PTT and PDT. Pharmaceutics 14, 1817.

Ma R., Alifu N., Du Z., Chen S., Heng Y., Wang J., Zhu L., Ma C., Zhang X., 2021. Indocyanine green-based theranostic nanoplatform for NIR fluorescence

image-guided chemo/photothermal therapy of cervical cancer. Int J Nanomedicine 16, 4847.

Ma Y.-Y., Jin K.-T., Wang S.-B., Wang H.-J., Tong X.-M., Huang D.-S., Mou X.-Z., 2017. Molecular imaging of cancer with nanoparticle-based theranostic probes. Contrast Media Mol Imaging 2017.

Macedo L.B., Nogueira-Librelotto D.R., Mathes D., de Vargas J.M., da Rosa R.M., Rodrigues O.E.D., Vinardell M.P., Mitjans M., Rolim C.M.B., 2021. Overcoming MDR by Associating Doxorubicin and pH-Sensitive PLGA Nanoparticles Containing a Novel Organoselenium Compound—An In Vitro Study. Pharmaceutics 14, 80.

Mallidi S., Luke G.P., Emelianov S., 2011. Photoacoustic imaging in cancer detection, diagnosis, and treatment guidance. Trends Biotechnol 29, 213–221.

Mehtala J.G., Kulczar C., Lavan M., Knipp G., Wei A., 2015. Cys34-PEGylated human serum albumin for drug binding and delivery. Bioconjug Chem 26, 941–949.

Mendes R., Pedrosa P., Lima J.C., Fernandes A.R., Baptista P. V., 2017. Photothermal enhancement of chemotherapy in breast cancer by visible irradiation of Gold Nanoparticles. Sci Rep 7, 1–9.

Ming Y., Wu N., Qian T., Li X., Wan D.Q., Li C., Li Y., Wu Z., Wang X., Liu J., 2020. Progress and future trends in PET/CT and PET/MRI molecular imaging approaches for breast cancer. Front Oncol 10, 1301.

Minotti G., Menna P., Salvatorelli E., Cairo G., Gianni L., 2004. Anthracyclines: molecular advances and pharmacologic developments in antitumor activity and cardiotoxicity. Pharmacol Rev 56, 185–229.

Mohanta V., Madras G., Patil S., 2012. Layer-by-layer assembled thin film of albumin nanoparticles for delivery of doxorubicin. The Journal of Physical Chemistry C 116, 5333–5341.

Moucheron C., 2009. From cisplatin to photoreactive Ru complexes: targeting DNA for biomedical applications. New journal of chemistry 33, 235–245.

Nomura S., Morimoto Y., Tsujimoto H., Arake M., Harada M., Saitoh D., Hara I., Ozeki E., Satoh A., Takayama E., 2020. Highly reliable, targeted photothermal cancer therapy combined with thermal dosimetry using a near-infrared absorbent. Sci Rep 10, 1–7.

Onishi T., Mihara K., Matsuda S., Sakamoto S., Kuwahata A., Sekino M., Kusakabe M., Handa H., Kitagawa Y., 2022. Application of magnetic

nanoparticles for rapid detection and in situ diagnosis in clinical oncology. Cancers (Basel) 14, 364.

Parodi A., Miao J., Soond S.M., Rudzińska M., Zamyatnin Jr, A.A., 2019. Albumin nanovectors in cancer therapy and imaging. Biomolecules 9, 218.

Pena B., Saha S., Barhoumi R., Burghardt R.C., Dunbar K.R., 2018. Ruthenium (II)-polypyridyl compounds with π-extended nitrogen donor ligands induce apoptosis in human lung adenocarcinoma (A549) cells by triggering caspase-3/7 pathway. Inorg Chem 57, 12777–12786.

Popolin C.P., Reis J.P.B., Becceneri A.B., Graminha A.E., Almeida M.A.P., Correa R.S., Colina-Vegas L.A., Ellena J., Batista A.A., Cominetti M.R., 2017. Cytotoxicity and anti-tumor effects of new ruthenium complexes on triple negative breast cancer cells. PLoS One 12, e0183275.

Poynton F.E., Bright S.A., Blasco S., Williams D.C., Kelly J.M., Gunnlaugsson T., 2017. The development of ruthenium (II) polypyridyl complexes and conjugates for in vitro cellular and in vivo applications. Chem Soc Rev 46, 7706–7756.

Rao W., Deng Z.-S., 2010. A review of hyperthermia combined with radiotherapy/chemotherapy on malignant tumors. Crit Rev Biomed Eng 38.

Rastrelli M., Tropea S., Rossi C.R., Alaibac M., 2014. Melanoma: epidemiology, risk factors, pathogenesis, diagnosis and classification. In Vivo (Brooklyn) 28, 1005–1011.

Sabhachandani P., Motwani V., Cohen N., Sarkar S., Torchilin V., Konry T., 2016. Generation and functional assessment of 3D multicellular spheroids in droplet based microfluidics platform. Lab Chip 16, 497–505.

Sainero-Alcolado L., Liaño-Pons J., Ruiz-Pérez M.V., Arsenian-Henriksson M., 2022. Targeting mitochondrial metabolism for precision medicine in cancer. Cell Death Differ 29, 1304–1317.

Sanità G., Armanetti P., Silvestri B., Carrese B., Cal G., Pota G., Pezzella A., d'Ischia M., Luciani G., Menichetti L., 2020a. Albumin-modified melanin-silica hybrid nanoparticles target breast cancer cells via a SPARC-dependent mechanism. Front Bioeng Biotechnol 8, 765.

Sanità G., Carrese B., Lamberti A., 2020b. Nanoparticle surface functionalization: How to improve biocompatibility and cellular internalization. Front Mol Biosci 7, 587012.

Sargazi S., Simge E.R., Gelen S.S., Rahdar A., Bilal M., Arshad R., Ajalli N., Khan M.F.A., Pandey S., 2022. Application of titanium dioxide nanoparticles in

photothermal and photodynamic therapy of cancer: An updated and comprehensive review. J Drug Deliv Sci Technol 103605.

Shahbazi-Gahrouei D., Khaniabadi P.M., Khaniabadi B.M., Shahbazi-Gahrouei S., 2019. Medical imaging modalities using nanoprobes for cancer diagnosis: A literature review on recent findings. J Res Med Sci 24.

Shi H., Sadler P.J., 2020. How promising is phototherapy for cancer? Br J Cancer 123, 871–873.

Shi Y., Zhu D., Wang D., Liu B., Du X., Wei G., Zhou X., 2022. Recent advances of smart AIEgens for photoacoustic imaging and phototherapy. Coord Chem Rev 471, 214725.

Siddique S., Chow J.C.L., 2020. Application of nanomaterials in biomedical imaging and cancer therapy. Nanomaterials 10, 1700.

Silva C.O., Pinho J.O., Lopes J.M., Almeida A.J., Gaspar M.M., Reis C., 2019. Current trends in cancer nanotheranostics: metallic, polymeric, and lipid-based systems. Pharmaceutics 11, 22.

Silvestri B., Armanetti P., Sanità G., Vitiello G., Lamberti A., Calì G., Pezzella A., Luciani G., Menichetti L., Luin S., 2019. Silver-nanoparticles as plasmon-resonant enhancers for eumelanin's photoacoustic signal in a self-structured hybrid nanoprobe. Materials Science and Engineering: C 102, 788–797.

Silvestri B., Vitiello G., Luciani G., Calcagno V., Costantini A., Gallo M., Parisi S., Paladino S., Iacomino M., D'Errico G., 2017. Probing the eumelanin–silica interface in chemically engineered bulk hybrid nanoparticles for targeted subcellular antioxidant protection. ACS Appl Mater Interfaces 9, 37615–37622.

Song M., Fu W., Liu Y., Yao H., Zheng K., Liu L., Xue J., Xu P., Chen Y., Huang M., 2021. Unveiling the molecular mechanism of pH-dependent interactions of human serum albumin with chemotherapeutic agent doxorubicin: A combined spectroscopic and constant-pH molecular dynamics study. J Mol Liq 333, 115949.

Sundquist T., Moravec R., Niles A., O'Brien M., Riss T., 2006. Timing your apoptosis assays. Cell Notes 16, 18–21.

Sung H., Ferlay J., Siegel R.L., Laversanne M., Soerjomataram I., Jemal A., Bray F., 2021. Global cancer statistics 2020: GLOBOCAN estimates of incidence and mortality worldwide for 36 cancers in 185 countries. CA Cancer J Clin 71, 209–249.

Tacar O., Sriamornsak P., Dass C.R., 2013. Doxorubicin: an update on anticancer molecular action, toxicity and novel drug delivery systems. Journal of pharmacy and pharmacology 65, 157–170.

Takata M., Murata H., Saida T., 2010. Molecular pathogenesis of malignant melanoma: a different perspective from the studies of melanocytic nevus and acral melanoma. Pigment Cell Melanoma Res 23, 64–71.

Tan R., Tian D., Liu J., Wang C., Wan Y., 2021. Doxorubicin-bound hydroxyethyl starch conjugate nanoparticles with pH/redox responsive linkage for enhancing antitumor therapy. Int J Nanomedicine 16, 4527.

Tasca E., Alba J., Galantini L., D'Abramo M., Giuliani A.M., Amadei A., Palazzo G., Giustini M., 2019. The self-association equilibria of doxorubicin at high concentration and ionic strength characterized by fluorescence spectroscopy and molecular dynamics simulations. Colloids Surf A Physicochem Eng Asp 577, 517–522.

Tchoryk A., Taresco V., Argent R.H., Ashford M., Gellert P.R., Stolnik S., Grabowska A., Garnett M.C., 2019. Penetration and uptake of nanoparticles in 3D tumor spheroids. Bioconjug Chem 30, 1371–1384.

Thorn C.F., Oshiro C., Marsh S., Hernandez-Boussard T., McLeod H., Klein T.E., Altman R.B., 2011. Doxorubicin pathways: pharmacodynamics and adverse effects. Pharmacogenet Genomics 21, 440.

Thota S., Rodrigues D.A., Crans D.C., Barreiro E.J., 2018. Ru (II) compounds: next-generation anticancer metallotherapeutics? J Med Chem 61, 5805–5821.

Tilsed C.M., Fisher S.A., Nowak A.K., Lake R.A., Lesterhuis W.J., 2022. Cancer chemotherapy: insights into cellular and tumor microenvironmental mechanisms of action. Front Oncol 12.

Tiruppathi C., Finnegan A., Malik A.B., 1996. Isolation and characterization of a cell surface albumin-binding protein from vascular endothelial cells. Proceedings of the National Academy of Sciences 93, 250–254.

Toussi A., Mans N., Welborn J., Kiuru M., 2020. Germline mutations predisposing to melanoma. J Cutan Pathol 47, 606–616.

Wahba H.A., El-Hadaad H.A., 2015. Current approaches in treatment of triple-negative breast cancer. Cancer Biol Med 12, 106.

Wang J.-Q., Yang Y., Cai C.-Y., Teng Q.-X., Cui Q., Lin J., Assaraf Y.G., Chen Z.-S., 2021. Multidrug resistance proteins (MRPs): Structure, function and the overcoming of cancer multidrug resistance. Drug Resistance Updates 54, 100743.

Wang L., Li D., Hao Y., Niu M., Hu Y., Zhao H., Chang J., Zhang Z., Zhang Y., 2017. Gold nanorod–based poly (lactic-co-glycolic acid) with manganese dioxide core–shell structured multifunctional nanoplatform for cancer theranostic applications. Int J Nanomedicine 12, 3059.

Wang T., Deng Y., Qu G., Chen Y., Shang J., Feng Z., Zheng J., Yang F., He N., 2019. Cell microarray chip system for accurate, rapid diagnosis and target treatment of breast cancer cells SK-BR-3. Chinese chemical letters 30, 1043–1050.

Weeks J.C., Catalano P.J., Cronin A., Finkelman M.D., Mack J.W., Keating N.L., Schrag D., 2012. Patients' expectations about effects of chemotherapy for advanced cancer. New England Journal of Medicine 367, 1616–1625.

Yang H., Villani R.M., Wang H., Simpson M.J., Roberts M.S., Tang M., Liang X., 2018. The role of cellular reactive oxygen species in cancer chemotherapy. Journal of Experimental & Clinical Cancer Research 37, 1–10.

Yang J., Zhang H., Chen B., 2016. Application of nanoparticles to reverse multi-drug resistance in cancer. Nanotechnol Rev 5, 489–496.

Yin Q., Shen J., Zhang Z., Yu H., Li Y., 2013. Reversal of multidrug resistance by stimuli-responsive drug delivery systems for therapy of tumor. Adv Drug Deliv Rev 65, 1699–1715.

Yu M., Zhang Y., Fang M., Jehan S., Zhou W., 2022. Current Advances of Nanomedicines Delivering Arsenic Trioxide for Enhanced Tumor Therapy. Pharmaceutics 14, 743.

Zeng C.-C., Lai S.-H., Yao J.-H., Zhang C., Yin H., Li W., Han B.-J., Liu Y.-J., 2016. The induction of apoptosis in HepG-2 cells by ruthenium (II) complexes through an intrinsic ROS-mediated mitochondrial dysfunction pathway. Eur J Med Chem 122, 118–126.

Zhang B., Wan S., Peng X., Zhao M., Li S., Pu Y., He B., 2020. Human serum albumin-based doxorubicin prodrug nanoparticles with tumor pH-responsive aggregation-enhanced retention and reduced cardiotoxicity. J Mater Chem B 8, 3939–3948.

Zhang D.-Y., Zheng Y., Tan C.-P., Sun J.-H., Zhang W., Ji L.-N., Mao Z.-W., 2017. Graphene oxide decorated with Ru (II)–polyethylene glycol complex for lysosome-targeted imaging and photodynamic/photothermal therapy. ACS Appl Mater Interfaces 9, 6761–6771.

Zhang L., Liu Y., Huang H., Xie H., Zhang B., Xi W., Guo B., 2022. Multifunctional nanotheranostics for near infrared optical imaging-guided treatment of brain tumors. Adv Drug Deliv Rev 114536.

Zhan P., Huang H., Huang J., Chen H., Wang J., Qiu K., Zhao D., Ji L., Chao H., 2015. Noncovalent ruthenium (II) complexes–single-walled carbon nanotube composites for bimodal photothermal and photodynamic therapy with near-infrared irradiation. ACS Appl Mater Interfaces 7, 23278–23290.

Zhang S.-Q., Meng T.-T., Li J., Hong F., Liu J., Wang Y., Gao L.-H., Zhao H., Wang K.-Z., 2019. Near-IR/visible-emitting thiophenyl-based Ru (II) complexes: efficient photodynamic therapy, cellular uptake, and DNA binding. Inorg Chem 58, 14244–14259.

Zhao J., Zhang Z., Wang X., 2020. Fabrication of pH-responsive PAA-NaMnF3@ DOX hybrid nanostructures for magnetic resonance imaging and drug delivery. J Alloys Compd 820, 153142.

Zheng X., Bian S., Liu W., Zhang C., Wu J., Ren H., Zhang W., Lee C.-S., Wang P., 2021. Amphiphilic Diketopyrrolopyrrole Derivatives for Efficient Near-Infrared Fluorescence Imaging and Photothermal Therapy. ACS Omega 6, 26575–26582.

Zhou J., Rao L., Yu G., Cook T.R., Chen X., Huang F., 2021. Supramolecular cancer nanotheranostics. Chem Soc Rev 50, 2839–2891.